PARTIAL UNMIXING OF HYPERSPECTRAL IMAGERY: THEORY AND METHODS

Jacob T. Mundt, GIS Mapping Coordinator
Ada County Weed Pest and Mosquito Abatement
5610 N Glenwood Street
Garden City, ID 83713
jmundt@adaweb.net

David R. Streutker, Research Assistant Professor
Nancy F. Glenn, Research Associate Professor
Boise Center Aerospace Laboratory
Idaho State University
322 E Front Street
Boise, ID 83702
stredavi@isu.edu
glennanc@isu.edu

ABSTRACT

The Minimum Noise Fraction (MNF) data reduction transform and Mixture Tuned Matched Filtering (MTMF) partial unmixing classification algorithm are relatively new image processing techniques that have proven to be effective target detection tools. These techniques allow partial unmixing and subpixel target abundance estimation, products that cannot be simultaneously achieved using standard mixture modeling or spectral angle mapping algorithms. This paper presents a tangible description of the technical background of both algorithms, a resource that is currently unavailable in existing literature. A demonstration of the use of the MNF and MTMF techniques is presented in detail for application to leafy spurge infestations in the Swan Valley, Idaho. The use of these techniques on hyperspectral imagery generated a producer's accuracy of 63% for infestations with canopy cover averaging 40% for imagery with 3.5 m resolution. Ramifications of image noise estimation and classification endmember selection are discussed at length and should be used as a resource guide for application to other vegetation studies.

INTRODUCTION

Previous literature has identified the Minimum Noise Fraction (MNF; Green *et al.,* 1988; Lee *et al*., 1990) data reduction transformation and the Mixture Tuned Matched Filtering (MTMF; Boardman, 1998) classification algorithm as a successful approach to partial unmixing and hyperspectral target identification. For example, Ben-Dor *et al.* (2001) used MTMF classifications of endmembers derived from high spatial resolution Compact Airborne Spectrograph Imager (CASI) data to characterize urban features, generating accuracies of 76%. Other studies have utilized MTMF to map geologic features with high success, finding subpixel mineral abundances as low as 5% (Boardman, 1998). Further, Kruse *et al.* (2003) determined enough confidence in MTMF classifications of geologic features to use the products as validation for other sensors. This study details descriptions of the MNF and MTMF algorithms and presents applied methods and discussion of MTMF detection of leafy spurge (*Euphorbia esula* L.), a target of significant remote sensing interest.

Leafy spurge is an invasive plant that has been listed as a noxious weed in many parts of the United States (Prather *et al.*, 2002; Galitz, 1980). Previous work by Parker-Williams and Hunt (2004) determined that MNF and MTMF processing methods were capable of detecting leafy spurge infestations with canopy cover as low as 10% with Producer's accuracies between 75% and 95%. Other work by Dudek *et al.* (2004) used MTMF methods applied to moderate spatial resolution hyperspectral data (20 m pixels) over Theodore Roosevelt National Park to temporally monitor leafy spurge (Producer's accuracies between 35% and 70%), and attribute lower accuracies in their study to the small spatial extent and highly fragmented nature of leafy spurge infestations in the study area. Glenn *et al.* (2005) documented repeatability in discrimination of leafy spurge, more accurately identifying small and fragmented leafy spurge infestations using MTMF applied to higher spatial resolution hyperspectral data (Producer's accuracies between 61% and 88%).

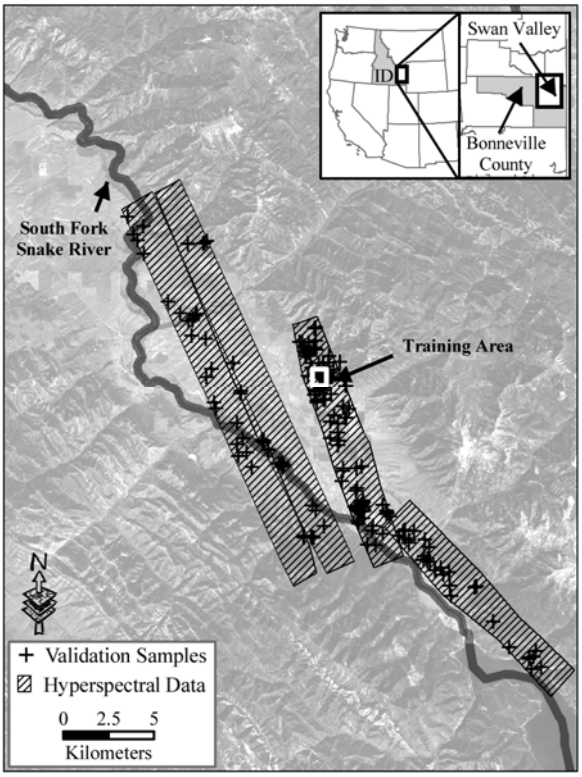

Figure 1. Location of the study area illustrating the hyperspectral scene and validation plot locations in the Swan Valley, Idaho.

The demonstration area for this study was located in the Swan Valley, Idaho, just west of the Idaho-Wyoming border (Figure 1). While most leafy spurge infestations in the study area were small (< 75 m^2, averaging approximately 40% cover), a few larger infestations (multiple hectares at high percent cover) demonstrated the potential for leafy spurge to aggressively invade the region. On June 29, 2003, four HyMap scenes (HyVista, 2005) were collected over the study area approximately two hours prior to solar noon. The data consisted of 126 spectral bands between 450 and 2500 nm, with bandwidths of approximately 15 nm and a spatial resolution of 3.5 m × 3.5 m. Each hyperspectral scene was approximately 1.8 km wide, and all scenes totaled nearly 60 km in length.

TECHNICAL BACKGROUND

The following section describes the MNF and MTMF algorithms conceptually and presents a succinct mathematical context. However, this manuscript is not intended to provide foundational mathematical concepts (which are well presented in referred literature) or specific computational routines (which are protected intellectual property). While the descriptions and equations presented herein were derived based on the ENvironment for Visualizing Images (ENVI) software (ITT-VIS, Boulder, CO) processing routines and documentation (ITT-VIS Personal Communication, 2005; ITT-VIS, 2003), it must be noted that the context of this discussion is more applicable to general MNF and MTMF understanding than to the specific ramifications of the software implementation.

Data Reduction

Previous work has documented various approaches to data reduction and noise correction. For example, Lee (1980) describes a noise filtering technique based on neighborhood mean and variance that does not require data transformation. Later work by Green *et al.* (1988) and Lee *et al.* (1990) developed the foundations of the MNF transform as described herein. Green *et al.* (1988) developed the concept of the maximum noise fraction transform, or data reorganization based on signal to noise ratio, and demonstrated noise filtering via complex matrix inversion. Lee *et al.* (1990) more clearly defined the maximum noise fraction transform as a two-phase principal component analysis transform (PCA; Davis, 1986) and documented the applicability of this technique to noise reduction in high spectral resolution data. Their study described data transformation such that the noise covariance matrix is reduced to an identity matrix, and subsequently applied principal components transform to noise projected data.

The first phase of the MNF transform can be described in five discrete steps, each of which is discussed below. These steps are: 1) determination of image noise, 2) calculation of the image noise covariance matrix and subsequent eigen-decomposition, 3) image mean correction, 4) decorrelation of the noise in the image, and 5) normalization of the linear noise in the data (noise whitening). The product of these linear transformations is a mean-corrected and noise-whitened data set, which is subsequently rotated using a standard PCA transform in the second phase of the MNF transform.

The MNF transform requires knowledge of the noise in the input data. Noise can either be determined directly using dark current measurements or through estimation (*e.g.,* shift difference calculations). Dark current measurements are at-sensor measured errors that can be directly subtracted from data, but they are not always available. When dark current data is not available or is not used, shift difference estimates may be utilized. Shift difference calculations are derived using a modified high frequency filter approach (Lillesand and Kiefer, 2000), as illustrated in Equation 1. Once the noise matrix is estimated, it is used to generate a noise covariance matrix using

the approach described in Equation 2. In the following text, matrices are noted as upper case letters encased in square brackets (*e.g.*,[*C*]), while vectors are noted as lower case letters with an arrow overshadow (*e.g.*, $\vec{e}$).

$$\left[N_{i,j,k}\right] = \frac{\left[D_{i,j,k}\right] - \left[D_{i-1,j,k}\right] + \left[D_{i,j,k}\right] - \left[D_{i,j-1,k}\right]}{2} \tag{1}$$

where [*N*] is the resulting three-dimensional noise matrix, [*D*] is the input three-dimensional data matrix, *i* and *j* range from 2 to the number of samples and lines, respectively, and *k* ranges from 1 to the number of bands, *b*.

$$\left[C_{\alpha,\beta}\right] = \frac{\sum_{p=1}^{np}\left(\left(\left[N_{p,\alpha}\right] - m_{\alpha}\right) \times \left(\left[N_{p,\beta}\right] - m_{\beta}\right)\right)}{np - 1} \tag{2}$$

where [*C*] is the noise covariance matrix, α and β range from 1 to *b*, *np* is the number of pixels in each band, and *m* is the band mean (for band α or β, respectively).

The resulting covariance matrix is subsequently decomposed into a b × b eigenvector matrix [E_n] and an eigenvalue vector $\vec{e}$. Noise eigenvalues characterize the dimensionality of the covariance matrix and represent the noise variance of each composite band, while noise eigenvectors distribute values into linearly independent composite bands (Davis, 1986; Nicholson, 1986). Because noise estimates are treated as a number of pixels by number of bands matrix in the noise covariance matrix calculation (Equation 2), the total number of pixels used in the shift difference calculation must be equal to or greater than the total number of bands transformed. Shift difference estimates are typically calculated over a subset of the reflectance data where there is minimal spectral variability (*e.g.,* deep, clear water or image calibration panels). If the shift difference technique is applied over an area that contains coherent signal variance, partial coherent signal may be misinterpreted as noise. Although it is assumed that this error would be small, the effect of signal degradation from noise misinterpretation in highly convex systems (Boardman, 1993) has not been quantified.

Following noise covariance calculation, input data are mean corrected and noise whitened. Mean correction is the subtraction of the mean (band) spectral reflectance from each pixel in its respective band (similar to low frequency filtering; Lillesand and Kiefer, 2000). Mean correction is useful because it defines the average image spectra as background, and spectrally unique features will depart from background values. It follows that if a target occurs in great abundance within the hyperspectral dataset, partial target signatures may be interpreted as background, confusing ensuing spectral classifications. As such, MNF and MTMF may not be optimal methods to map large scale features, such as land cover types.

The mean-corrected image data is noise whitened in two steps. First, it is projected onto the image noise eigenvectors, thereby decorrelating the noise in the data and redistributing the noise decorrelated data into linearly independent composite bands. Second, each band is normalized to the square root of its corresponding noise eigenvalue, rescaling the data into unit noise standard deviations. As a result of this normalization, each data value within the image is a statistical measure of its deviation from the zero mean. Mean correction and noise whitening are mathematically summarized by Equation 3:

$$\left[W\right] = \left[R\right] \# \left[E_n\right] \# \left(\left[D_{np,b}\right] - m_b\right)^T \tag{3}$$

where [*W*] is the resulting mean-corrected, noise-whitened three-dimensional dataset, [*R*] is a diagonal matrix with elements equal to the reciprocals of the square roots of $\vec{e}$, [$D_{\mathrm{np,b}}$] represents [*D*] as a two-dimensional matrix (number of pixels by number of bands), and m_b is the mean of band *b*. (In these equations, the "#" symbol represents the projection operator.)

The final step of the MNF transform is a standard PCA rotation, which projects the noise-whitened, mean-corrected data onto its own covariance eigenvectors and reorders the data bands by decreasing band variance. This step is done in the standard manner as described above, and is mathematically summarized by Equation 4:

$$\left[MNF\right] = \left[T\right] \# \left[W\right] \tag{4}$$

where [*MNF*] is the final MNF output in units of noise standard deviations and [*T*] is the b × b eigenvector matrix derived from [*W*].

Transformed MNF data have several unique and simple properties: they are band decorrelated, have a zero mean, and have unit noise variance. The covariance matrix of an MNF transformed dataset is a diagonal matrix with elements equal to the MNF eigenvalues. The MNF eigenvalues decrease sequentially by band and have a lower bound of one, due to unit noise variance. Because noise eigenvectors have been directly correlated to signal-to-noise ratios, MNF transforms are generally more effective at signal component organization than PCA rotations (Green *et al.*, 1988).

Image Classification

Over the last 20 years, various approaches to image classification have been derived, many of which also estimate subpixel target components. Unlike traditional linear spectral unmixing methods (Lillesand and Kiefer, 2000), several of these approaches seek to minimize interference and develop a relative measure of similarity between pixel spectra and target spectra. Harsanyi and Chang (1994) documented an Orthogonal Subspace Projection (OSP) approach to the simultaneous data reduction and classification of hyperspectral data. In a two step process, they first project spectra onto the vector orthogonal to the undesirable targets, and subsequently project the residuals onto the target spectra, producing a component image representing the distribution of the target feature. From this, Tu *et al.* (1998) developed a Noise Subspace Projection (NSP) approach to image classification which does not require covariance matrix inversion, making it useful in the analysis of hyperspectral data. Other work by Pinzón *et al.* (1998) documented a Hierarchal Foreground Background Analysis (HFBA) approach to linear unmixing of spectral data that minimized extraneous noise by developing a series of weighting vectors which extracted important discriminating features. Finally, Asner and Lobell (2000) document an automated approach to unmixing reflectance from soils and vegetation, and used a Monte Carlo approach to estimate errors in derived subpixel cover fractions.

The Mixture Tuned Matched Filtering algorithm consists of two phases, a Matched Filter calculation for abundance estimation and a Mixture Tuning calculation for the identification and rejection of false positives. Matched Filtering was originally developed for use in electrical and signal processing (Henderson and Lewis, 1998). In an optical remote sensing context, Matched Filtering can be described as the process of filtering the input data for good matches to the target spectrum while suppressing the remaining background spectra. Matched filtering is mathematically equivalent to the Constrained Energy Minimization described by Harsayni (1993) (ITT-VIS, Personal Communication). The segregating power in the MTMF algorithm is in the Mixture Tuning, which calculates a value of infeasibility (or a measure of goodness of match) for each MF classified pixel. The MTMF algorithm as described here implicitly requires zero mean, unit noise variance input data (such as MNF transformed data) for proper Mixture Tuning calculation.

Matched Filter scores are calculated for each pixel by projecting the MNF transformed data onto a Matched Filter Vector. This vector is derived by transforming the target spectrum into MNF space (using the process described above), projecting it onto the inverse covariance of the MNF data, and normalizing it to the magnitude of the target spectrum. This ensures that the Matched Filter Vector has unit length and corresponds to target components ranging from 0% to 100%. The mathematical definition of the Matched Filter Vector is summarized in Equation 5:

$$\vec{v} = \frac{\left[C_{MNF}\right]^{-1} \# \vec{t}_{MNF}}{(\vec{t}_{MNF})^{T} \# \left[C_{MNF}\right]^{-1} \# \vec{t}_{MNF}} \tag{5}$$

where $\vec{v}$ is the Matched Filter Vector, $[C_{MNF}]^{-1}$ is inverse of the MNF covariance matrix (a diagonal matrix of eigenvalue reciprocals) and $\vec{t}_{MNF}$ is the vector of the target spectra in MNF space. Matched Filter values are subsequently calculated for each pixel (creating an $i \times j$ target abundance image) by projecting the MNF transformed data onto the Matched Filter Vector $\vec{v}$, as expressed in Equation 6:

$$\left[MF\right] = \vec{v} \ \# \ \left[MNF\right] \tag{6}$$

Output MF scores are normally distributed and have a mean of zero, where the magnitude of the MF score represents the linear solution to the MF projection. MF values of zero and lower represent background (no target

component), and pixels with a MF score greater than zero are considered to contain a fractional target component equivalent to the MF score. Systems with low spectral contrast (Okin *et al.*, 2001) may have increased potential for spectral confusion, which may introduce irregularity in output MF scores, possibly resulting in MF scores greater than one. These high MF scores may be an artifact of target variability, or may occur as unique mixtures of background materials that falsely represent the target spectra.

The Mixture Tuning portion of the MTMF algorithm assesses the probability of an MF estimation error for each pixel, based on the concept of mixing feasibility. The calculation of infeasibility value of each pixel takes place over three distinct steps: 1) determination of the target vector component of the pixel, 2) interpolation of variance eigenvalues respective to the target vector component, and 3) calculation of the standardized separation between a pixel and its ideal target vector component. The target vector component of a pixel is the scalar product of its MF score and the target vector, as illustrated in Equation 7:

$$\vec{c}_i = MF_i \times \vec{t}_{MNF} \tag{7}$$

where $\vec{c}_i$ is the target vector component for pixel *i* and MF_i is the Matched Filter value of the pixel. An ideal pixel, containing some fraction of the target, will lie directly on the target vector (Figure 2; Pixel **X**). Actual pixels, however, will likely contain some degree of noise variance and background mixing, resulting in a pixel that does not lie directly on the target vector (Figure 2; Pixels **Y** and **Z**). The proximity of each pixel to its idealized location on the target vector is a conceptual measure of infeasibility.

As described above, the units of MNF-space are defined in terms of noise standard deviations. Thus the proximity of a pixel's actual location to its ideal projected location (on the target vector) is a statistical measure of its spectral variance from the target. Pixels with high percent target component are expected to have a low degree of mixing freedom (low variance) because their spectral characteristics should be dominated by the target. Alternatively, pixels with low percent target component are expected to have a higher degree of mixing freedom (high variance) because they mix with combinations of background components to form varied spectral signatures. Because pixels with small target vector components have higher degrees of mixing freedom than do pixels with large target vector components, it is necessary to establish variance thresholds to consistently assess acceptable degrees of data variance based on mixing freedom. For example, an MNF value of four may be considered unreasonably high for a pixel with a MF score of 0.9 but acceptable for a pixel with a MF score of 0.1. For this reason, measures of data variance are standardized based on estimates of mixing feasibility. The mathematical derivation of infeasibility requires eigenvalue interpolation and is determined following Equation 8.

$$\vec{e}_i = \left(\sqrt{\vec{e}_{MNF}} - MF_i \times \left(\sqrt{\vec{e}_{MNF}} - \vec{e}_n\right)\right)^2 \tag{8}$$

where $\vec{e}_i$ is the interpolated vector of eigenvalues for pixel i, $\vec{e}_{MNF}$ is the vector of MNF eigenvalues, and $\vec{e}_n$ is the vector of MNF noise eigenvalues (a vector of ones).

These standardizations (variance thresholds) are determined by the linear interpolation of eigenvalues between the 100% target distribution (eigenvalues are all equal to one, having no mixing freedom and therefore only unit noise variance) and the 100% background distribution (eigenvalues generally much greater than one, representative of high degrees of mixing freedom) (Figure 2). The infeasibility value of a pixel is calculated as the geometric distance from the pixel to the target vector, normalized to the variance threshold magnitude for the respective MF value. The mathematical derivation of infeasibility values is illustrated in Equation 9.

$$I_i = \frac{\left\|\vec{s}_i - \vec{c}_i\right\|}{\left\|\vec{e}_i\right\|} \tag{9}$$

where I_i is the resulting infeasibility value for pixel *i*, and $\vec{s}_i$ is the MNF spectra for pixel i.

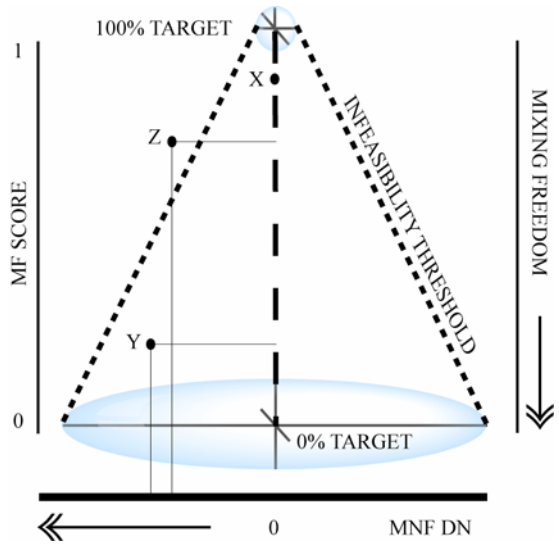

Figure 2. Mixture Tuning cone of infeasibility illustrating increasing eigenvalue threshold with increasing mixing freedom for three eigenvalue-constrained, orthogonal MNF axes. Modified from ITT-VIS (2003).

This mixture-tuning portion of MTMF generates a value that represents the statistical distance from the target-mixing vector for each pixel, and can be directly interpreted as a measure of mixing feasibility. An example is shown in Figure 2. Though pixel **Y** has a larger noise variance than pixel **Z**, it also has a higher allowed mixing freedom. As a result, pixel **Y** falls within the feasibility cone, while pixel **Z** does not (*i.e.*, pixel **Y** has lower infeasibility than pixel **Z**), and as such, is interpreted as background rather than as target.

APPLIED METHODS

MTMF processing methods generally estimate noise, extract spectral endmembers, and classify scenes independently of each other. In this study, however, only one of the four collected data scenes had a known leafy spurge infestation that was suitable for use as a training site (geographically large and with high percent leafy spurge cover). Consequently, each scene was MNF transformed utilizing the same noise statistics in order to optimize the utility of the training area. Using the same set of noise statistics for all scenes ensured that all data were projected into the same MNF space and a single training endmember was appropriate for all classifications. Spectral bands 63, 64, and 126 (at wavelengths of 1406 nm, 1420 nm, and 2493 nm, respectively) were not analyzed because of decreased data coherence due to atmospheric water absorption, and further processing was applied to the remaining 123 reflectance bands.

Data Reduction

This study calculated image noise estimates using the shift difference technique. The effect of image noise estimation techniques (*i.e.,* size and location of the area used for noise estimation) was constrained using a 512 × 640 pixel subset of the imagery containing agricultural fields, conifer trees, shrubs, grasslands, and a relatively large (~170 pixels, or ~2000 m^2) leafy spurge infestation. Within the subset, three spatially independent areas were used for noise estimation (each larger than the 123 pixel minimum requirement). The first noise estimate was calculated over a 13 × 13 pixel area within a grass pasture, the second over a 60 × 40 pixel area within a wheat field, and the third was derived from the entire 512 × 640 pixel subset. Three independent MNF transformations were derived using the three different noise estimates, and were characterized by MNF eigenvalue maximums of 11,943, 2,297, and 82 for the grass pasture, wheat, and entire subset estimations, respectively.

The inverse relationship between the number of pixels used to estimate noise and maximum MNF eigenvalue is interpreted to be due to lower signal variance within geographically smaller ecosystems. That is, noise estimates derived from smaller, more homogenous areas have lower total variance, and implicitly, lower noise estimates as compared to larger, more diverse areas. Smaller MNF eigenvalues are correlated to lower variance in output MNF bands. Because the full scene noise estimation produced the lowest eigenvalues, it is inferred that some coherent signal was interpreted as noise. It follows that there was likely some misinterpretation of signal when estimating noise from the smaller areas as well. This misinterpretation may be at the scale of continuum removal when considering noise estimated from large areas, or at the micro-scale when considering noise estimated from smaller areas. Because there is some uncertainty as to which noise estimation method may be more appropriate, preliminary leafy spurge MTMF classifications were evaluated using each of the three MNF transformed subsets for comparison. For consistency, each dataset was classified to map only high percent cover leafy spurge infestations (> 50% cover). A minimum MF value of 0.5 and a maximum infeasibility value of 20 were used to generate the desired classifications (detailed processing methods are presented in subsequent discussions).

For this study, it was concluded that noise estimates using the entire subset had both lower values of infeasibility and less spectral confusion (spatial scatter) than classifications resulting from the other two subsets (see results section). As such, full scene (approximately 2×10^6 pixels) noise estimations were used for subsequent data processing.

The appropriate number of MNF bands to use in further analyses was determined by evaluating the visible coherence in the MNF dataset as well as the behavior of bivariate plots of MNF eigenvalues, inverse eigenvalues, and cumulative MNF eigenvalues. Ultimately, the first 70 MNF bands (approximately 90% of the cumulative MNF variance) were used for further processing. This threshold provided high confidence that all coherent data were included in the classification, while eliminating 53 bands (43% of the dataset) as noise dominated.

Endmember Selection

Previous work documents methods for determining endmembers and endmember variance (Bateson and Curtiss, 1996; Bateson *et al.*, 2000). In this study, leafy spurge endmembers were determined using the spectral Pixel Purity Index (PPI) rotation and N-Dimensional Visualization (N-DV) algorithms applied to a 200 × 200 pixel subset containing the leafy spurge training site. The PPI rotation can be conceptualized as a modified Low Probability Detection approach (Tu *et al.*, 1998), with n-dimensional datasets being iteratively collapsed onto random two-dimensional unit vectors, where pixels at the end of these vectors (extreme pixels) represent low probability targets. In this study, 30,000 iterations at a PPI threshold of 2.5 produced approximately 39,000 (of 40,000) pixels designated as extreme in at least one projection. Of these, approximately 34,000 were discarded because they composed the lower 90% of the cumulative PPI frequency distribution (PPI minimum threshold of 200).

Leafy spurge formed a distinct endmember cluster in the ND-V (using the 5000 pixels resolved from the PPI), and 113 leafy spurge endmember pixels were isolated (Figure 3). The use of ND-V output is an interactive method to derive training pixels for classification; however, in this study it was difficult to justify which pixel(s) to choose as the 'correct' training endmember(s). Using multiple random ND-V projections, four distinct pixels were isolated that were all extreme representations of leafy spurge (one for each of four distinct projections; boxed pixels in Figure 3).

This study investigated the effect of endmember selection by classifying the image using three distinct methods: 1) N-DV endmembers - 4 extreme pixels selected from four random N-DV projections, 2) mean endmember - average of all 113 extreme endmember pixels, and 3) user guided endmember - the average of 4 pixels selected using field data. The N-DV endmembers represented the variability within the leafy spurge community (similar to discussions presented by Batesman and Curtiss (1996)). The user-guided endmember represented methods commonly utilized in image processing, and was the same endmember utilized by Glenn *et al.* (2005).

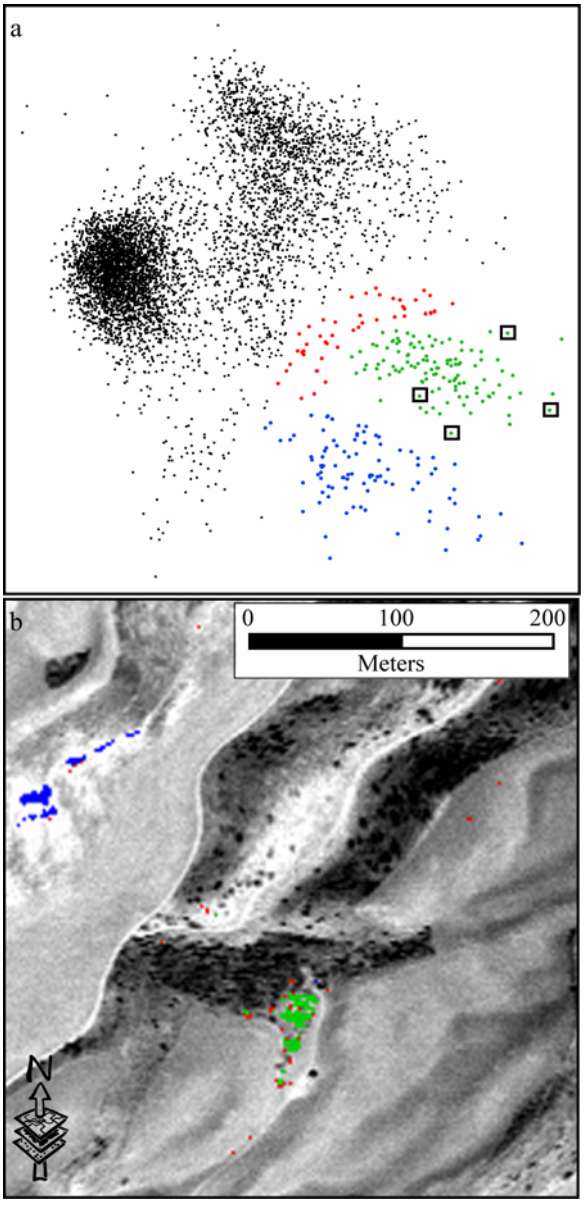

Figure 3. a) An N-Dimensional Visualization of leafy spurge endmember (green). Additionally, mixed pixels containing some leafy spurge and some background (red) and spectrally similar vegetation that is not leafy spurge (blue) are indicated. b) The geographic distribution of each of the colored groups in (a), with the leafy spurge training area dominated by 113 green pixels. Boxed pixels represent extreme endmembers used for classification.

Image Classification

For each of the endmembers, MTMF produced one MF image and one infeasibility image. These data were evaluated using scatterplots of MF score versus infeasibility value (Figure 4). For this study, MF scores of zero and less were interpreted as background, and scores greater than one were interpreted as high percent target reflectance (~100%). Using the scatterplot, pixels with MF scores greater than

zero and infeasibility values below 20 were considered to potentially contain leafy spurge. The maximum infeasibility threshold (20) was determined iteratively using values measured in known occurrences of leafy spurge over the training area and was later confirmed using other Global Position System (GPS) validated locations. Based on the scatterplots, it was determined that lower values of MF required lower values of infeasibility than did higher values of MF. For example, a pixel with a MF score of 0.9 and an infeasibility value of 10 most commonly represented leafy spurge, while a pixel with an MF score of 0.25 and an infeasibility value of 10 most commonly represented background (Figure 4). It can be inferred from Figure 4 that the convexity of leafy spurge mixing generally prohibits the differentiation of leafy spurge from background at MF scores less than 0.35; however, some pixels with low MF scores are differentiable, given that they have very low values of infeasibility. The scatterplots were evaluated iteratively and produced pixels classified as leafy spurge that were exported into a Geographic Information System (GIS) for accuracy assessment.

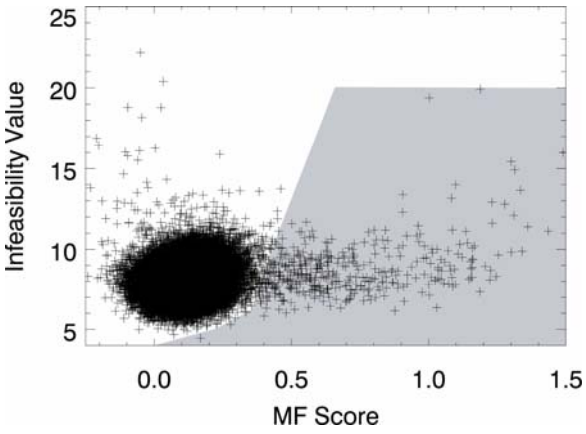

Figure 4. Scatterplot of MF scores versus infeasibility values resulting from an MTMF classification. The pixels within the shaded area were classified to contain leafy spurge.

Accuracy Assessment

In this study, Trimble GeoXT GPS receivers (Trimble; Sunnyvale, CA) were used to collect 214 GPS polygon validation samples (differentially corrected to sub-meter accuracy) representing both leafy spurge presence (flowering and non-flowering shoots; 68 plots) and absence (146 plots in mixed ecology). One hundred and seventy-seven samples were collected in the summer of 2003, and 37 additional samples collected in the summer of 2004. GPS-derived validation plots were buffered by 15 m to accommodate geometric error in the imagery. Accuracy assessment followed methods described by Congalton and Green (1999) and Foody (2004). Detailed descriptions of the field validation and accuracy assessment procedures used are presented by Glenn *et al.* (2005).

The correlation of MF scores to field estimated leafy spurge cover was evaluated in addition to assessing classification at the presence/absence level. Correlations were only assessed with true positive validation polygons. Of the 68 positive validation polygons, 43 were classified as true positives using the most effective classification strategy as defined by accuracy assessments (discussion to follow). Twenty-six of these 43 polygons contained at least one classified pixel, while the remaining 17 were considered true positives because they were within 15 m of a predicted leafy spurge location. The 26 GPS-derived polygons that included classified points within their boundaries were commonly associated with larger infestations and higher percent cover than the remaining 17 polygons.

RESULTS

Data Reduction

Classifications resulting from grass pasture, wheat, and entire subset noise estimates produced 86, 206, and 214 pixels classified as leafy spurge present, respectively. In the case of the classification resulting from the grass pasture noise estimates, all 86 pixels corresponded to known infestations of leafy spurge, however many pixels known to contain leafy spurge in high abundance were not classified. Further inspection demonstrated that most of the unclassified pixels containing leafy spurge had infeasibility values ranging between 40 and 100, which, after iterative processing, was determined to be higher than acceptable. For this reason, the classification produced using the noise from the grass pasture was not evaluated further. Values of infeasibility in the classification resulting from wheat and entire subset noise estimations were significantly lower (less than 20).

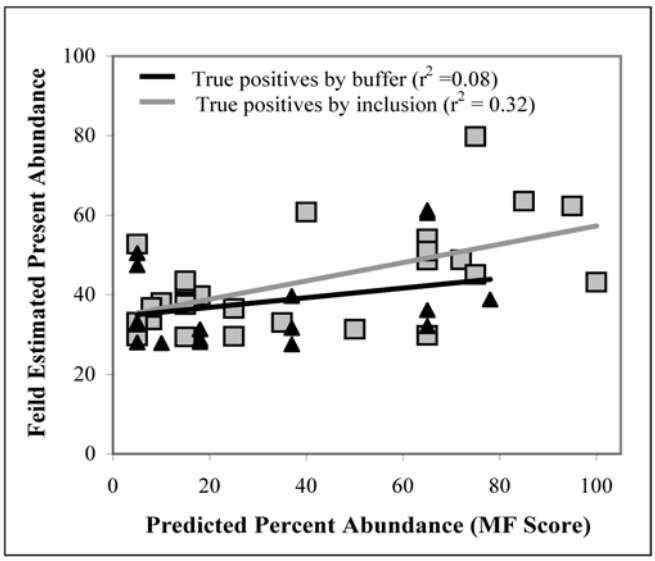

Figure 5. Regression analysis between calculated MF score and field observed abundance (canopy cover). Boxes represent true positive infestations by inclusion, while triangles represent pixels classified as true positives by buffering.

Table 1. Classification Accuracies

Classification Strategy	Producer's Accuracy	User Accuracy	Overall Accuracy
Extreme 1	41%	90%	80%
Extreme 2	53%	90%	83%
Extreme 3	41%	80%	78%
Extreme 4	51%	76%	79%
Mean Selected	63%	88%	86%
Mean Calculated	54%	86%	82%
Extreme Combined	60%	71%	79%
Number of Positives		68	
Number of Negatives		146	

For the wheat subset, 206 pixels were mapped as leafy spurge present, while 214 pixels were mapped in the classification resulting from entire subset noise estimation. In both subsets, 182 pixels classified as leafy spurge were interpreted as correctly classified (based on field knowledge of the area). All residual classified pixels not within a two pixel buffer (7 m) of a correctly classified pixel were considered false positives. It is notable that this 7 m buffer is independent of the 15 m buffer used in classification accuracy assessment (described above), because the noise estimates test only relative accuracy and are not affected by geometric imprecision.

Of the remaining entire subset noise classification pixels, 28 of 32 were located within 7 m of a correctly classified pixel, while only 5 of the 24 wheat noise classification pixels were within this buffer. This indicates that the wheat noise estimation generated a classification with higher levels of confusion than did the entire subset noise estimation, even when considering only high percent cover infestations (MF > 0.5). Statistical testing applied to the 182 correctly classified pixels demonstrated no significant difference in MF scores between the two classifications. Values of infeasibility from the classification derived using wheat noise estimates, however, were significantly higher than values of infeasibility derived from the classification using the entire subset for noise estimates (t-test, 95% confidence interval; Davis, 1986). It is interesting to note that while higher MNF eigenvalues typically represent higher information content (Kruse *et al.*, 2003), in this study, higher MNF eigenvalues resulted in lower classification accuracy.

Image Classification

The user-guided leafy spurge endmember generated Producer's, User, and overall accuracies of 63%, 88%, and 86%, respectively, while the mean endmemeber resulted in Producer's, User and overall accuracies of 54%, 86%, and 82% (Table 1). The four individual N-DV endmembers generated Producer's accuracies between 41% and 53%, User accuracies between 76% and 90%, and overall accuracies between 78% and 83% (Table 1). Qualitative evaluation indicated that extreme endmember classifications were complimentary (*e.g.,* leafy spurge infestations missed by one extreme endmember classification were identified by a different extreme endmember), which was not unexpected following work by Batesman *et al.* (2000). This hypothesis was supported in that a combined (merged) extreme endmember classification generated Producer's, User, and overall accuracies of 60%, 71%, and 79%, respectively.

Regression analysis of all MF scores produced by the most effective classification (user-guided) with the oblique field estimates of leafy spurge cover produced a weak relationship (r^2 = 0.24; Figure 5). The 26 validation polygons containing classification points had an r^2 value of 0.32, higher than that of the remaining 17 validation polygons classified as true positives due to buffering (r^2 = 0.08). These correlation coefficients both independently failed to reject the null hypothesis that they were due to chance at 90% confidence (Davis, 1986).

DISCUSSION

The User accuracies for leafy spurge detection were consistently high in this study, but the Producer's accuracies were lower than desired. Previous work by Glenn *et al.* (2005) and Mundt *et al.* (2005) demonstrate that this reduced accuracy is likely dependent on the small size and low percent cover of infestations in the study area. Although the Producer's accuracies are low, the classification is useful for management needs as the User accuracy is high enough to provide a decision support tool for leafy spurge management.

Endmember selection in hyperspectral processing is a critical analysis step that commonly is not adequately addressed in reports. MTMF calls for the most 'pure' spectral endmember to be used for classification training; however, a distinction must be made between what is 'pure', what is 'extreme', and what is appropriate. In this study, different classification endmembers generated over 20% variability in Producer's accuracy. The most appropriate endmember for classification in this study was the average (mean) of a small group of pixels with high percent target cover, though these pixels were not the most obvious extreme pixels in n-dimensional space.

While the N-DV extreme endmembers may be considered spectrally unique and are likely to contain a leafy spurge component, they may not represent pure leafy spurge (*i.e.,* each endmember may be dominantly leafy spurge mixed with differing background components) (Bateson and Curtiss, 1996). It is interpreted that combining N-DV endmembers coalesced the endmember variability and effectively mapped the dominant leafy spurge signature. However, this process did increase classification noise, as illustrated by a slight decrease in User accuracy compared with other classifications. The accuracies generated from the combined extreme endmember classification are similar to the accuracies from the user-guided endmember classification. Visual comparison supported the hypothesis that the user-guided endmember classification outperformed the combined extreme endmember classification, as there was less spatial scatter.

In terms of the MTMF algorithm, the use of more than one N-DV endmembers conceptually generates overlapping infeasibility cones around multiple target vectors, each with a slightly different target spectrum. This effectively results in a single, inflated infeasibility pseudo-cone that encompasses all individual cones, and certain pixels within the volume of overlap are classified by multiple endmembers. This pseudo-cone increases spectral confusion by artificially lowering infeasibility scores for spectrally similar (non-leafy spurge containing) pixels, thereby erroneously classifying them as target present.

Infeasibility values generated by MTMF were useful in the reduction of false positives, thereby increasing accuracies over Matched Filtering alone. This result, also replicated in other studies (*e.g.*, Dudek *et al.*, 2004), demonstrates the advantage of the MTMF algorithm as compared to CEM or OSP. It is notable that pixels with high MF score were more clearly interpreted as leafy spurge present or absent than were pixels with a lower MF score. Vegetative systems have been documented to mix in a nonlinear fashion (Roberts *et al.,* 1993; Borel and Gerstl, 1994; Ray and Murray, 1998), thus implying that linear solutions incorporated by the MTMF algorithm are potentially restrictive. While leafy spurge in the Swan Valley is a relatively new and generally poorly established invader, many pixels in the scene have both MF scores greater than one and relatively low infeasibility values. It is possible that the effects of nonlinear mixing may be amplified at lower percent cover infestations, with Figure 4 illustrating how the maximum acceptable infeasibility threshold may vary depending on MF score. This relationship is important for highly fragmented or small infestations because they become more difficult to effectively classify. Future work could address the relationship between the MF score and values of infeasibility to further automate the selection of true positive pixels and may necessitate the re-evaluation of the linear interpolation of mixing feasibility thresholds. Additionally, future work could focus on converting the measure of goodness from values of infeasibility to values of probability, which is a more widely understood and generally useful quantification.

While previous work has demonstrated strong correlations between MF scores and percent target component (*e.g.,* Parker Williams and Hunt, 2002), this study did not produce such relationships. We hypothesize that multiple data collection personnel and temporal variability in data collection contributed to reduced r^2 values. Further, perimeters of infestations may be diffuse and coverage classes within an infestation are commonly variable. As a result, multiple field personnel may potentially interpret a field validation plot differently. Finally, previous work documents variance in classified subpixel estimates (in some cases, greater than 20%) and attributes this inconsistency to what has been presented herein as endmember variability (Asner and Lobell, 2000; Bateson *et al.*, 2000; Roberts *et al*., 1993).

Data reduction and noise estimation in hyperspectral data analysis have received significant attention in the last 20 years, and in the future it is certain that new algorithms will continue to develop. In general, image noise can be described in three components: instrumental, atmospheric, and photonic. Noise estimates derived using dark current data will consider only instrument noise, but not any residual atmospheric or photonic noise. Alternatively, noise estimates derived using the shift difference technique will estimate the total image noise; however, this estimate is

restricted to a linear solution that may fail to accommodate nonlinear noise components (*e.g.,* signal-dependent photonic noise or topography-dependent atmospheric noise). Additionally, because the number of pixels used to calculate the image noise must be equal to or greater than the number of bands in the transformed dataset (when using the shift difference technique), an unknown amount of natural variance will be included in the noise estimates, regardless of the subset size used. Ultimately, these factors introduce some uncertainty as to how appropriately the MNF transform is able to accommodate noise, and future studies may consider how to more accurately estimate and accommodate these various noise types. Using spectral calibration panels may reduce this error, though rarely are such targets placed over geographic areas large enough to provide the necessary number of pixels. The impact of partial noise removal will likely depend on project objectives; however, the authors stress that for application-based studies, MNF transformed data and MTMF classifications continue to perform adequately. While MTMF classifications are somewhat subjective (as are many image classification methods), it should be noted that, with experience, analysts are commonly able to develop a processing flow that enables the production of quality, repeatable results.

CONCLUSIONS

This study presented details of the Minimum Noise Fraction transform and the Mixture Tuned Matched Filtering classification algorithm. These algorithms were used to locate spatially small occurrences of leafy spurge in a mixed grass environment to Producer's accuracies between 41% and 63% and User accuracies between 71% and 90% (Table 1). Noise estimates were evaluated using three different target areas, with the best estimate produced by using the larger, more ecologically diverse subset. The use of individual and multiple target endmembers was also investigated, with the highest accuracies from a classification made using an endmember derived from the mean of several manually selected target pixels.

ACKNOWLEDGEMENTS

This project was funded by the NASA BAA program (NASA Stennis, NAG13-02029). We thank Mr. William Graham of NASA Stennis for his continued support. Additional support was provided by NASA Goddard (NAG5-12301), NOAA Environmental Technology Laboratory, and the INL-ISU Partnership for Integrated Environmental Analysis Education Outreach Program. The authors would like to acknowledge the Weed Control Crew from Bonneville County, Idaho, Mr. Mark Strom and Ms. Charlla Adams from Boise State University for their assistance with field data collection, and Mr. Keith Weber from Idaho State University for helping prepare this manuscript. Finally, the authors would like to acknowledge ITT-VIS for providing access to the theoretical foundations of the MNF and MTMF algorithms implemented in ENVI.

REFERENCES

Asner, G.P. & Lobell, D.B. (2000). A biogeophysical approach for automated SWIR unmixing of soils and vegetation. *Remote Sensing of Environment, 74,* 99-112.

Bateson, A. & Curtiss, B. (1996). A method for manual endmember selection and spectral unmixing. *Remote Sensing of Environment, 55*, 229-243.

Bateson, A., Asner, G.P. & Wessman, C.A. (2000). Endmember bundles: A new approach to incorporating endmember variability into spectral mixture analysis. *IEEE Transactions on Geoscience and Remote Sensing, 38(2)*, 1083-1094.

Ben-Dor, E., Levin, N. & Saaroni, H. (2001). A spectral based recognition of the urban environment using the visible and near-infrared spectral region (0.4-1.1 µm). A case study over Tel-Aviv, Israel. *International Journal of Remote Sensing, 22(11)*, 2193-2218.

Boardman, J.W. (1993). Automating spectral unmixing of AVIRIS data using convex geometry concepts. In: *Summaries of The Fourth Annual JPL Airborne Geoscience Workshop*, JPL Publication 93-26, Vol. 1, pp. 11-14. Arlington, VA.

Boardman, J.W. (1998). Leveraging the high dimensionality of AVIRIS data for improved sub-pixel target unmixing and rejection of false positives: Mixture Tuned Matched Filtering. In: *Proceedings of the 7th Annual JPL Airborne Geoscience Workshop,* JPL Publication 97-1, pp. 55. Pasadena, CA.

Borel, C.C. & Gerstl, S.A.W. (1994). Nonlinear spectral mixing models for vegetative and soil surfaces. *Remote Sensing of Environment*, 47, 403-416.

Congalton, R.G. & Green, K. (1999). *Assessing the Accuracy of Remotely Sensed Data: Principles and Practices.* (137 pages). Lewis Publishers: Boca Raton, FL.

Davis, J.C. (1986). *Statistics and Data Analysis in Geology, 2nd edn*. (646 pages). John Wiley & Sons: New York, NY.

Dudek, K.B., Root, R.R., Kokaly, R.F., Anderson, G.L., Brown, K.E., Mladinich, C.S., Stitt, S.F., Hager, S.N., & Lefsky, M.A. (2004). Temporal monitoring of leafy spurge: An example using 1999 and 2001 Airborne Visible/Infrared Imaging Spectrometer (AVIRIS) data over Theodore Roosevelt National Park. In: *Proceedings of the Society for Range Management 57th Annual Meeting*. Society for Range Management, Salt Lake City, UT.

Foody, G.M. (2004). Thematic map comparison: Evaluating the statistical significance of differences in classification accuracy. *Photogrammetric Engineering & Remote Sensing, 70(5)*, 627-633.

Galitz, D.S. (1980). A summary of the synonymy of leafy spurge. In: *North Dakota Research Report # 77,* North Dakota State University, pp. 6.

Glenn, N.F., Mundt, J.T., Weber, K.T., Prather, T.S., Lass, L.W., & Pettingill, J. (2005). Hyperspectral data processing for repeat detection of small infestations of leafy spurge. *Remote Sensing of Environment, 95(3)*, 399-412.

Green, A.A., Berman, M., Switzer, P., & Craig, M.D. (1988). A transformation for ordering multispectral data in terms of image quality with implications for noise removal. *Transactions on Geoscience and Remote Sensing, 26(1)*, 65-74.

Harsanyi, J.C. (1993). *Detection and Classification of Subpixel Spectral Signatures in Hyperspectral Image Sequences*, Ph.D. Dissertation, University of Maryland, Baltimore County, 116 pp.

Harsanyi, J.C. & Chang, C. (1994). Hyperspectral image classification and dimensionality reduction: An orthogonal subspace projection approach. *IEEE Transactions on Geoscience and Remote Sensing, 32*, 779-785.

HyVista. (2005). Airborne Hyperspectral Surveys and Information Products. URL: http://www.hyvista.com/main.html, Accessed December, 2005.

Kruse F.A., Boardman, J.W. & Hunnington, J.F. (2003). Comparison of airborne hyperspectral data and EO-1 Hyperion for mineral mapping. *IEEE Transactions on Geoscience and Remote Sensing*, *41(6)*, 1388-1400.

Lee, J. (1980). Digital image enhancement and noise filtering by use of local statistics. *IEEE Transactions on Pattern Analysis and Machine Intelligence, PAMI-2*, 165-168.

Lee J.B., Woodyatt, S. & Berman, M. (1990). Enhancement of high spectral resolution remote sensing data by a noise-adjusted principal components transform. *IEEE Transactions on Geoscience and Remote Sensing, 28(3),* 295-304.

Lillesand, T.M. & Kiefer, R.W. (2000). *Remote Sensing and Image Interpretation, 4th edn*. (724 pages). John Wiley & Sons, Inc: New York, NY.

Mundt, J.T., Glenn, N.F., Weber, K.T., Prather, T.S., Lass, L.W., & Pettingill, J. (2005). Discrimination of hoary cress and determination of its detection limits via hyperspectral image processing and accuracy assessment techniques. *Remote Sensing of Environment, 96*, 509-517.

Nicholson, K.W. (1986). *Elementary Linear Algebra with Applications.* (476 pages). PWS Publishers: Boston, MA.

Okin, G.S., Roberts, D.A., Burray, B., & Okin, W.J. (2001). Practical limits on hyperspectral vegetation discrimination in arid and semiarid environments. *Remote Sensing of Environment, 77,* 212-225.

Parker-Williams, A. & Hunt, E.R. (2002). Estimation of leafy spurge cover from hyperspectral imagery using Mixture Tuned Matched Filtering. *Remote Sensing of Environment, 82*, 446-456.

Parker-Williams, A. & Hunt, E.R. (2004). Accuracy assessment for detection of leafy spurge with hyperspectral imagery. *Journal of Range Management, 57*, 106-112.

Pinzon, J.E., Ustin, S.L., Castaneda, C.M., & Smith, M.O. (1998). Investigation of leaf biochemistry by Hierarchical Foreground / Background Analysis. *IEEE Transactions on Geoscience and Remote Sensing, 36(6),* 1913-1927.

Prather, T.S., Robins, S.S., Morishita, D.W., Lass, L.W., Callihan, R.H. & Miller, T.W. (2002) *Idaho's Noxious Weeds,* University of Idaho, Moscow, ID.

Ray, T.W. & Murray, B.C. (1998). Nonlinear spectral mixing in desert vegetation. *Remote Sensing of Environment, 55,* 59-64.

Roberts, D.A., Smith, M.O. & Adams, J.B. (1993). Green vegetation, nonphotosynthetic vegetation, and soils in AVIRIS data. *Remote Sensing of Environment*, 44, 255-269.

ITT-VIS (2003). ENVI User Guide, Boulder, Colorado: ITT Visual Information Solutions.

Tu, T., Chen, C. & Chang, C. (1998). A noise subspace projection approach to target signature detection and extraction in an unknown background for hyperspectral images. *IEEE Transactions on Geoscience and Remote Sensing 36(1):* 171-181.